

## CANGAROO-III OBSERVATIONS OF THE SUPERNOVA REMNANT RX J0852.0–4622

R. ENOMOTO<sup>1</sup> S. WATANABE<sup>2</sup> T. TANIMORI<sup>2</sup> A. ASAHARA<sup>2</sup> G. V. BICKNELL<sup>3</sup> R. W. CLAY<sup>4</sup> P. G. EDWARDS<sup>5</sup> S. GUNJI<sup>6</sup>  
S. HARA<sup>7</sup> T. HATTORI<sup>8</sup> S. HAYASHI<sup>9</sup> Y. HIGASHI<sup>2</sup> R. INOUE<sup>8</sup> C. ITOH<sup>10</sup> S. KABUKI<sup>2</sup> F. KAJINO<sup>9</sup> H. KATAGIRI<sup>11</sup> A. KAWACHI<sup>8</sup>  
S. KAWASAKI<sup>1</sup> T. KIFUNE<sup>1</sup> R. KIUCHI<sup>1</sup> K. KONNO<sup>9</sup> L. KSENOFONTOV<sup>1</sup> H. KUBO<sup>2</sup> J. KUSHIDA<sup>8</sup> Y. MATSUBARA<sup>12</sup>  
T. MIZUKAMI<sup>2</sup> R. MIZUNIWA<sup>8</sup> M. MORI<sup>1</sup> H. MURAIISHI<sup>13</sup> T. NAITO<sup>14</sup> T. NAKAMORI<sup>2</sup> D. NISHIDA<sup>2</sup> K. NISHIJIMA<sup>8</sup> M. OHISHI<sup>1</sup>  
Y. SAKAMOTO<sup>8</sup> V. STAMATESCU<sup>4</sup> S. SUZUKI<sup>15</sup> T. SUZUKI<sup>15</sup> D. L. SWABY<sup>4</sup> H. TANIMURA<sup>2</sup> G. THORNTON<sup>4</sup> F. TOKANAI<sup>6</sup>  
K. TSUCHIYA<sup>2</sup> Y. YAMADA<sup>9</sup> M. YAMAZAKI<sup>9</sup> S. YANAGITA<sup>15</sup> T. YOSHIDA<sup>15</sup> T. YOSHIKOSHI<sup>1</sup> M. YUASA<sup>1</sup> Y. YUKAWA<sup>1</sup>

*To appear in ApJ main journal.*

### ABSTRACT

Sub-TeV gamma-ray emission from the North-West rim of the supernova remnant RX J0852.0–4622 was detected with the CANGAROO-II telescope and recently confirmed by the H.E.S.S. group. In addition, the H.E.S.S. data revealed a very wide (up to two degrees in diameter), shell-like profile of the gamma-ray emission. We have carried out CANGAROO-III observations in January and February 2005 with three telescopes and show here the results of three-fold coincidence data. We confirm the H.E.S.S. results about the morphology and the energy spectrum, and find the energy spectrum in the NW-rim is consistent with that of the whole remnant.

*Subject headings:* gamma rays: observation — supernova remnant: individual (RX J0852.0–4622)

### 1. INTRODUCTION

RX J0852.0–4622 (G266.2–1.2) is one of the few supernova remnants (SNRs) from which strong non-thermal X-ray emission has been detected (Aschenbach 1998; Tsunemi et al. 2000; Slane et al. 2001). A distance of  $\sim 200$  pc and an age of  $\sim 700$  years (Aschenbach et al. 1999; Tsunemi et al. 2000) would make RX J0852.0–4622 one of the closest young SNR (although see Slane et al. 2001, for a dissenting view). The non-thermal emission suggests particle acceleration to  $\sim 100$  TeV, with the possibility of TeV gamma-ray emission from inverse Compton scattering off electrons, and/or  $\pi^0$  decay from proton interactions, with clear implications for the origin of cosmic rays in our galaxy

(Völk et al. 2005).

Sub-TeV gamma-rays from the northwest rim (NW rim) of RX J0852.0–4622 were detected with the 10 m CANGAROO-II imaging atmospheric Cherenkov telescope (IACT) (Katagiri et al. 2005). Gamma-ray emission was recently confirmed by the H.E.S.S. group (Aharonian et al. 2005b), who mapped the spatial distribution of gamma-ray emission over the whole remnant, using data from at least two of four telescopes in their array.

RX J0852.0–4622 is the second spatially resolved SNR at TeV gamma-ray energies (Enomoto et al. 2002; Aharonian et al. 2004). The CANGAROO-II result indicated a soft energy spectrum  $\propto E^{-4.3^{+1.7}_{-4.4}}$ , however, in contrast the H.E.S.S. group reported a harder spectrum  $E^{-2.1 \pm 0.1 \pm 0.2}$ . The gamma-ray fluxes also appeared discrepant: at 1 TeV the CANGAROO-II flux level was 15% of the Crab nebula, whereas the H.E.S.S. result was 100% of the Crab. The clear differences between these two reports are;

- CANGAROO-II was only sensitive to within  $0.4^\circ$  of the X-ray maximum in the NW rim (Aschenbach 1998; Tsunemi et al. 2000; Slane et al. 2001) whereas H.E.S.S. was sensitive to the whole remnant.
- the CANGAROO-II observation used a single telescope whereas the H.E.S.S. observations used stereo data from two or more telescopes.
- the CANGAROO-II flux was derived based on the subtraction of a background derived from the surrounding area which included part of the remnant, whereas the H.E.S.S. background was derived from an off-source region outside the remnant. The CANGAROO-II result, therefore, was dependent on the spatial distribution of gamma-rays inside the SNR.

The H.E.S.S. result (from stereo observations) showed very extended emission, up to one degree in radius from

<sup>1</sup> Institute for Cosmic Ray Research, University of Tokyo, Kashiwa, Chiba 277-8582, Japan

<sup>2</sup> Department of Physics, Graduate School of Science, Kyoto University, Sakyo-ku, Kyoto 606-8502, Japan

<sup>3</sup> Research School of Astronomy and Astrophysics, Australian National University, ACT 2611, Australia

<sup>4</sup> Department of Physics and Mathematical Physics, University of Adelaide, SA 5005, Australia

<sup>5</sup> Paul Wild Observatory, CSIRO Australia Telescope National Facility, Locked Bag 194, Narrabri, NSW 2390, Australia

<sup>6</sup> Department of Physics, Yamagata University, Yamagata, Yamagata 990-8560, Japan

<sup>7</sup> Ibaraki Prefectural University of Health Sciences, Ami, Ibaraki 300-0394, Japan

<sup>8</sup> Department of Physics, Tokai University, Hiratsuka, Kanagawa 259-1292, Japan

<sup>9</sup> Department of Physics, Konan University, Kobe, Hyogo 658-8501, Japan

<sup>10</sup> National Institute of Radiological Sciences, Chiba, Chiba 263-8555, Japan

<sup>11</sup> Department of Physical Science, Graduate School of Science, Hiroshima University, Higashi-Hiroshima, Hiroshima 739-8526, Japan

<sup>12</sup> Solar-Terrestrial Environment Laboratory, Nagoya University, Nagoya, Aichi 464-8602, Japan

<sup>13</sup> School of Allied Health Sciences, Kitasato University, Sagami-hara, Kanagawa 228-8555, Japan

<sup>14</sup> Faculty of Management Information, Yamanashi Gakuin University, Kofu, Yamanashi 400-8575, Japan

<sup>15</sup> Faculty of Science, Ibaraki University, Mito, Ibaraki 310-8512, Japan

the center of the remnant. In this paper we present the results of CANGAROO-III stereoscopic observations and determine how much of the apparent discrepancies between these two earlier results arise from these differences.

## 2. CANGAROO-III STEREOSCOPIC SYSTEM

The use of imaging atmospheric Cherenkov telescopes (IACTs) was established with the statistically unassailable detection of the Crab nebula at TeV energies by the Whipple group (Weekes et al. 1989). This technique enables TeV gamma-rays to be selected from the huge background of cosmic rays with the use of the ‘‘Hillas parameters’’ of the shower images (Hillas 1985). Stereoscopic observations, which allow the signal-to-noise ratio to be significantly improved, were pioneered by the HEGRA group (Aharonian et al. 1999). The H.E.S.S. group has recently reported the detection of faint gamma-ray sources with an angular resolution as fine as a few arc-minutes (Aharonian et al. 2005).

CANGAROO-III is one of two major IACTs located in the southern hemisphere. The CANGAROO-III stereoscopic system consists of four imaging atmospheric Cherenkov telescopes located near Woomera, South Australia (31°S, 137°E). Each telescope has a reflector of 10 m diameter. Each reflector consists of 114 segmented spherical mirrors (80 cm in diameter with a radius of curvature of 16.4 m) made of FRP (Kawachi et al. 2001) mounted on a parabolic frame ( $f/d=0.77$ , i.e., a focal length of 8 m). The total light collection area is 57.3 m<sup>2</sup>. The first telescope, T1, which was the CANGAROO-II telescope, is not presently in use due to its smaller field of view and higher energy threshold. The second, third, and fourth telescopes (T2, T3, and T4) were used for the observations described here. The camera systems for T2, T3, and T4 are identical and their details are given in Kabuki et al. (2003). The telescopes are located at the east (T1), west (T2), south (T3) and north (T4) corners of a diamond with sides of  $\sim 100$  m (Enomoto et al. 2002b).

## 3. OBSERVATIONS

The observations were carried out in the period from 2005 January 16 to February 23 using ‘‘wobble mode’’ in which the pointing position of each telescope was shifted in declination between  $\pm 0.5$  degree from the center of the remnant (RA, dec = 133.00°,  $-46.37^\circ$  J2000) every 20 minutes (Daum et al. 1997). Data were recorded for T2, T3 and T4 when more than four photomultiplier (PMT) signals exceeded 7.6 photoelectrons (p.e.) in any two telescopes (‘‘Global Trigger’’) (Nishijima et al. 2005). The typical trigger rate was 9 Hz for three-fold coincidence. Each night was divided into two or three periods, i.e., ON-OFF, OFF-ON-OFF, or OFF-ON observations. ON-source observations were timed to contain the meridian passage of the target. On average the OFF source regions were located with an offset in RA of  $+30^\circ$  or  $-30^\circ$  from the center of the remnant. The OFF-source observations were also made in wobble mode. The total observation time was 1736 and 1408 min, for ON and OFF observations, respectively. Next we required the images in all three telescopes to have clusters of at least five adjacent pixels exceeding a 5 p.e. threshold (three-fold coincidence). The event rate was reduced to  $\sim 6$  Hz

by this criterion. Looking at the time dependence of these rates, we can remove data taken in cloudy conditions. This procedure is the same as the ‘‘cloud cut’’ used in the CANGAROO-II analysis (Enomoto et al. 2002). We also rejected data taken at elevation angles less than  $60^\circ$ . In total, 1081 min. data survived these cuts for ON and 1031 min. for OFF, with a mean elevation angle of  $70.3^\circ$ . The size of this supernova remnant is large (2 degree) even compared to the field of view (FOV) of our observation (4 degree). One of the reason why we took ‘‘wobble’’ observation is to enlarge the effective FOV, the other is to average the responses of individual pixels. We, therefore, took LONG OFF source run of ‘‘wobble’’ mode for background subtractions in the later analysis.

Prior to these observations, we observed this SNR from 2004 January to February with two telescopes (T2 and T3). and preliminary results can be found in Tanimori et al. (2005). The statistics of the OFF-source runs were insufficient, only 1/3 of the ON-source runs. Therefore, we describe that data set in the Appendix and concentrate on the description of 2005 observations in the body of this paper.

The light collecting efficiencies, including the reflectivity of the segmented mirrors, the light guides, and the quantum efficiencies of photomultiplier tubes were monitored by a muon-ring analysis (Enomoto et al. 2006). The light yield per unit arc-length is approximately proportional to the light collecting efficiencies. The ratios of these at the observation period with respect to the mirror production times (i.e., deterioration factors) were estimated to be 45, 55, and 73% for T2, T3, and T4, respectively. The measurement errors are considered to be at less than the 5% level. These values were checked analyzing Crab data which were obtained in 2004 November, which are described in the next section. The deteriorations were mostly due to dirt and dust settling on the mirrors. We cleaned the mirrors with water in October 2005 and the partial improvement (a factor of 1.3-1.4) of the light collecting efficiencies were observed.

## 4. ANALYSIS

The analysis procedures used were identical with those described in Enomoto et al. (2006) for the Vela pulsar wind nebula, which is approximately 0.5 degree south of the Vela Pulsar. As a full instrumental description was given in Enomoto et al. (2006), we omit a detailed discussion here.

At first, the Hillas parameters (Hillas 1985) were calculated for the three telescopes’ images. The gamma-ray incidence directions were adjusted by minimizing the sum of squared widths (weighted by the photon yield) of the three images seen from the assumed position (fitting parameter).

In order to derive the gamma-ray likeliness, we used an established mathematical method, the Fisher Discriminant (hereafter  $FD$  in short) (Fisher 1936). When we use a multi-parameter set such as:

$$\vec{P} = (W2, W3, W4, L2, L3, L4),$$

where  $W2, W3, W4, L2, L3, L4$  are energy corrected *widths* and *lengths* for the T2, T3, and T4 and assume that a linear combination of

$$FD = \vec{\alpha} \cdot \vec{P},$$

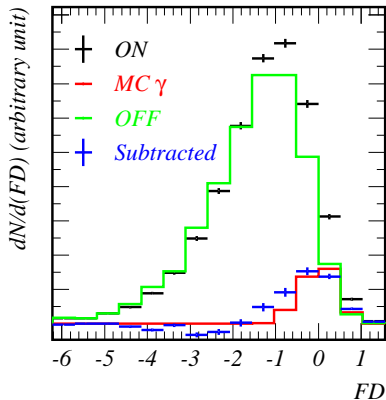


FIG. 1.— Fisher Discriminant ( $FD$ ) distributions. The black points with the error bars are those for events inside a one degree circle centered on the SNR. The green histogram is for OFF-source data. The normalization of the latter was determined by the fitting procedure described in the text. The blue points show the background subtracted signals and the red histogram is the best fit for gamma-rays from Monte-Carlo simulations.

provides the best separation between signal and background, then the set of linear coefficients ( $\vec{\alpha}$ ) should be uniquely determined as

$$\vec{\alpha} = \frac{\vec{\mu}_{sig} - \vec{\mu}_{BG}}{E_{sig} + E_{BG}},$$

where  $\vec{\mu}$  is a vector of the mean value of  $\vec{P}$  for each sample and  $E$  is their correlation matrix. This method is widely used in the high-energy experiments such as the  $B - factory$  in order to separate spherical events from jet-like ones (Abe et al. 2001). We previously used it in Vela Pulsar analysis (Enomoto et al. 2006) to separate “sharp” (gamma-ray-like) images from “smeared” (background) ones. The values of  $\vec{\mu}_{sig}$ ,  $\vec{\mu}_{BG}$ ,  $E_{sig}$ , and  $E_{BG}$  can be calculated from the Monte-Carlo and observational data (OFF-source runs), respectively.

$FD$  is a linear combination of multi-parameters. We, therefore, should select parameters which can be linearly added. The *widths* and *lengths* of T2, T3, and T4 are second order cumulative moments of shower images and thus their linear combination is a reasonable assumption. In order to keep the mean of the Hillas parameters (which are energy dependent) at the same values in various energies, we corrected the energy dependence of each parameter subtracting best-fitted second-order polynomials for the Monte-Carlo gamma-rays, i.e., the means of the corrected Hillas parameters are all set to zero for gamma-rays, independent of energy. This procedure ensures the mean position of the  $FD$  to be located at zero for gamma-rays. Also a linear combination of six random parameters ensures the distribution has an approximately Gaussian form (see the red histogram in Fig. 1 of Monte-Carlo gamma-ray events). The contributions of Hillas parameters to the photon-proton separation can be expressed by  $\alpha_i \cdot P_i$ , which were (0.06, 0.25, 0.48, 0.28, 0.31, 0.16) for  $W2$ ,  $W3$ ,  $W4$ ,  $L2$ ,  $L3$ ,  $L4$ , respectively.

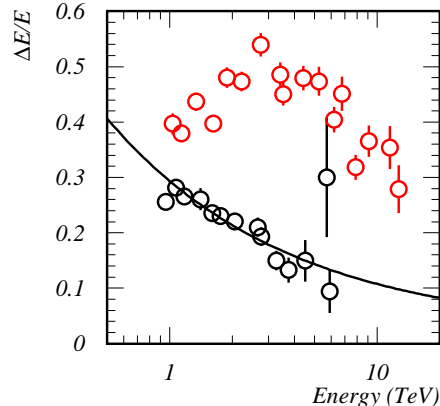


FIG. 2.— The energy resolution ( $\Delta E/E$ ) estimated by Monte-Carlo simulations. The red points are obtained before the “edge cut” and the black points after it. The curve is the best-fit function described in the text.

The main differences of three telescopes are the different spot sizes of mirrors. As was expected, the *width* of T4 gave the largest contribution which reflects the respective mirror qualities. The  $FD$  can be understood as an approximate representation of “mean scaled *width*” which was energy corrected and linearly corrected by the other Hillas parameters. The advantage of this method is that it can be calculated fully automatically in the analysis procedure, i.e., any IACT can reproduce it.

Here, we rejected events with hits in the outermost layer of the cameras (“edge cut”). These rejected events cause finite deformations especially in the *length* distribution which results in deformations of the  $FD$ . This cut was introduced after the analysis in Enomoto et al. (2006) and was found to improve the energy resolution significantly:  $\Delta E/E$  was estimated using Monte-Carlo simulations and is plotted in Fig. 2. The red points are those before the “edge cut” and the black after. A dramatic improvement in energy resolution is obtained. It was parametrized by the function  $\Delta E/E = 27/\sqrt{E/1 TeV} + 2\%$  (the solid curve in Fig. 2.). Here, we did not apply either the “core distance” or “slant distance” corrections described in Hofmann et al. (2000). The gamma-ray energies were simply estimated by the total number of photoelectrons observed. Although this cut significantly reduces gamma-ray acceptance, especially in the higher energy region, we decided to use it in order to safely determine the gamma-ray energy spectrum in this analysis. The improvement of acceptance may be considered in more detail elsewhere in the future.

Since we have  $FD$  distributions for OFF-source data and the Monte-Carlo gamma-ray events, we can assume these are background and signal behaviors. We, therefore, can fit the  $FD$  distribution of ON (the black points in Fig. 1) with the above emulated signal and real background functions, to derive the number of signal events passing the selection criteria. With this fit, we can deter-

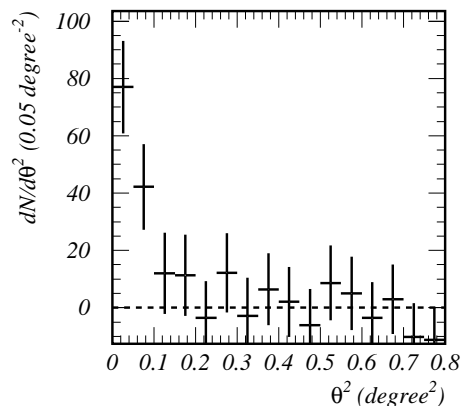


FIG. 3.— The  $\theta^2$  plot for the 2004 November Crab nebula data.

mine the gamma-ray excess without any positional subtractions, i.e., we can analyze all events in the FOV and not only the events which comes from the direction of the SNR. This is a two-parameter fitting and these coefficients can be exactly derived analytically. To summarize, there are two differences in the analysis procedure from the Vela paper (Enomoto et al. 2006);

- events with hits in the outermost layer were rejected (“edge cut”), and
- OFF-source events were used for emulating the background behavior of the  $FD$ .

In contrast, in the previous analysis, the background function was made from the ON data (outside of the source region), because of the lack of statistics of the OFF data. The  $FD$  has a position dependence and it deforms near the edge of camera. Thus with the high statistics OFF events, the current background determination is improved and its position dependence inside the FOV of the camera was taken into account. The result of the fitting is shown by the blue points (the background-subtracted signal) and the red histogram (the best-fit signal) in Fig. 1, while the green is the best-fit background. We have a statistically significant signal within one degree of the SNR center. Note that this fitting procedure gives a maximum acceptance with reasonably small statistical errors without introducing any image cuts, i.e., a  $\chi^2$  fit gives the maximum acceptance of events remaining after the pre-selections and automatically minimizes the subtraction ranges. In addition, it removes any subjective bias in cut determination.

This method was checked by analysis of Crab nebula data taken in November 2004. The wobble-mode observation was also used. The analyzable data corresponded to 316.4 min. The  $\theta^2$  plot is shown in Fig. 3. The number of excess events is  $119 \pm 22$  ( $5.4\sigma$ ). The flux is  $1.2 \pm 0.3$  times the standard Crab flux with the power-law consistent with the standard index of  $-2.5$ .

H.E.S.S. produced a very clean gamma-ray count map showing the shell-like structure of RX J0852.0–4622. In

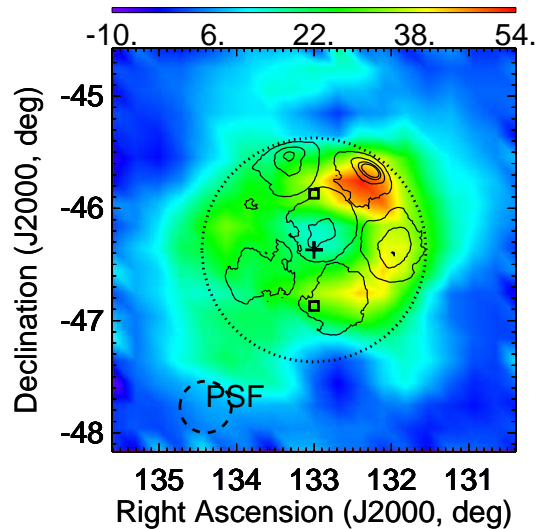


FIG. 4.— Morphology of gamma-ray-like events. The smoothing was carried out using the average of the center and neighboring eight pixel where pixel size was  $0.2 \times 0.2$  degree<sup>2</sup>. The vertical scale (number of events per pixel) is indicated in the top bar. The dotted circle of 1 degree from the supernova center is shown. The dashed circle of 0.23 degree (plotted in lower left) is the ( $1\sigma$ ) point spread function, where 68% of events are contained. The cross indicates the average pointing position, i.e., the center of the remnant and the squares the “wobble” pointing positions. The contours are the 20, 45, 65, and 80% levels in the ASCA Gas Imaging Spectrometer X-ray map (Tsunemi et al. 2000; Slane et al. 2001).

making a 2D-count map, we tried a simple time-based subtraction. The normalization factor for OFF-source run is  $1081/1031=1.05$ . We made two 2D-plots for arrival directions for ON and OFF using selected events with the  $FD$  in the range between  $-1$  and  $1$ , which is the signal region as shown in Fig. 1. The difference between two 2D distributions with the above normalization is shown in Fig. 4. Comparing it with Fig. 2 of Aharonian et al. (2005b), we confirm the shell-like structure, with less emission in the center position. Our data show that the emission in the northwest-rim (NW-rim) is the strongest. The signal-to-noise ratio (S/N) of our analysis is significantly worse than that of H.E.S.S., which can be seen comparing the S/N of Fig. 1 in Aharonian et al. (2005b) and Fig. 1 of this paper. Therefore, the statistical error in this map is larger than that in the H.E.S.S. map. The difference between red and green of this color map (Fig. 4) is not significant.

Fig. 4 was made by positional subtraction. Fig. 1 was made based on fitting the event shapes ( $FD$ ). We can also study the morphology by extracting gamma-ray-like events using the fitting procedure described so far. The  $FD$  distributions for each direction are recorded in multiple histograms and the fittings were carried out. The resulting morphology is shown in Fig. 5. Although we observe a shell-like structure, the brightest region has changed from that of Fig. 4. As has been described, the difference between this figure and Fig. 4 can be considered to be within the level of statistical fluctuations.

We have thus confirmed the H.E.S.S. results that RX J0852.0–4622 is a strong, shell-like TeV gamma-ray

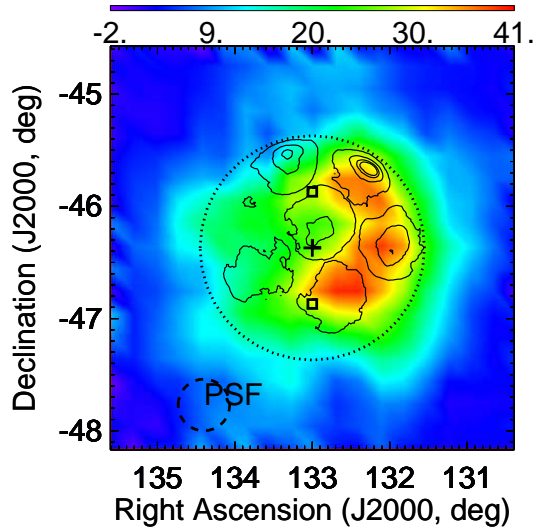


FIG. 5.— Morphology of gamma-ray-like events obtained by the fitting procedure described in the text. The other definitions are as same as those of Fig. 4.

source. We have also confirmed our previous claim of the CANGAROO-II detection of gamma-rays from the bright NW-rim (though not the reported soft spectrum). The threshold of this analysis (Figs. 1, and 4) is estimated to be 1.02 TeV. This high threshold can be explained by the deterioration of “light collection efficiencies”. The relatively poor S/N, even for the three-fold coincidence data, can be explained by the blur spot size of  $>0.1$  degree of the segmented mirrors, which are made of plastic. Monte-Carlo simulations with zero spot size show a much better separation between gamma-ray and proton events. This means that replacing these mirrors with glass or metal, we have a chance to approach H.E.S.S. quality even with 10 m diameter structure of the present telescopes.

## 5. RESULT

The radial distribution of the gamma-ray signal with respect to the SNR center is shown in Fig. 1 of Aharonian et al. (2005b). We took the  $FD$  distributions of annuli of various squared-radii with respect to the SNR center and fitted them. The  $\theta^2$  distribution over a wide range is shown in Fig. 6. The spatial excess appears only within one degree from the center of the SNR, in agreement with the H.E.S.S. result. The number of excess events is  $557 \pm 77$  ( $7.2\sigma$ ).

The gamma-ray fluxes within a one-degree radius were derived by fitting the  $FD$  distributions within this area on an energy bin-by-bin basis. The black squares in Fig. 7 are obtained by this experiment. The numerical data are listed in Table 1. The consideration on the experimental energy resolution was carried out unfolding the generated energy from the detected photon-electron yield using the Monte-Carlo events under the assumption that the energy spectrum is proportional to  $E^{-2.1}$  (H.E.S.S.’s spectrum). The “Mean Energy” quoted in Table 1 is the mean generated energy of the accepted

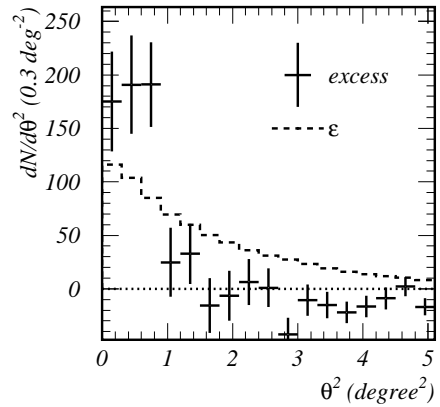


FIG. 6.— Wide-range  $\theta^2$  plot. The vertical scales are the numbers of excess events per  $0.3 \text{ degree}^2$ . The dashed histogram is the acceptance (in arbitrary units).

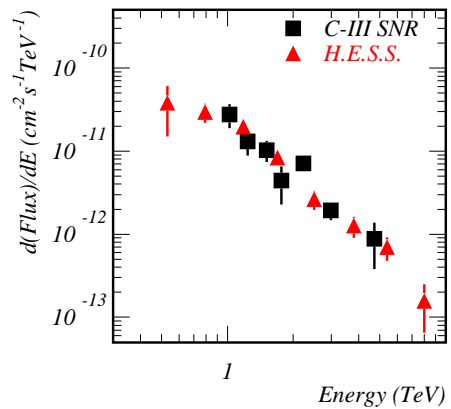


FIG. 7.— Differential energy spectra; the red points by H.E.S.S. are for the whole remnant and the black points from these CANGAROO-III observations are also for the whole remnant. The error bars are statistical.

TABLE 1  
DIFFERENTIAL FLUX WITHIN ONE DEGREE FROM THE SNR CENTER.

Energy binning (TeV)	Mean Energy (TeV)	dF/dE ( $\text{cm}^{-2}\text{s}^{-1}\text{TeV}^{-1}$ )
0.83 – 1.07	1.02	$(2.77 \pm 0.88) \times 10^{-11}$
1.07 – 1.37	1.24	$(1.32 \pm 0.43) \times 10^{-11}$
1.37 – 1.62	1.51	$(1.03 \pm 0.29) \times 10^{-11}$
1.62 – 1.91	1.77	$(4.40 \pm 2.14) \times 10^{-12}$
1.91 – 2.66	2.24	$(7.11 \pm 1.17) \times 10^{-12}$
2.66 – 3.70	2.98	$(1.93 \pm 0.46) \times 10^{-12}$
3.70 – 6.07	4.72	$(8.83 \pm 5.03) \times 10^{-13}$

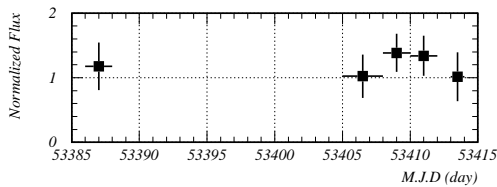


FIG. 8.— Time variability of the integral fluxes at the energy greater than 1.02 TeV. The vertical axis is the flux normalized to the H.E.S.S. mean flux ( $dF/dE = 2.1 \times 10^{-11} E^{-2.1}$  [ $\text{cm}^{-2}\text{s}^{-1}\text{TeV}^{-1}$ ]). The horizontal axis is modified Julian days (M.J.D.).

events in the Monte-Carlo simulation in each binning. The obtained differential flux is calculated at this "Mean Energy" under the assumption of the above power-law spectrum. The best fit with a power-law assumption for this energy spectrum is:

$$\frac{dF}{dE} = [2.5 \pm 0.6(\text{stat.}) \pm 0.6(\text{sys.})] \times 10^{-11} \cdot \left( \frac{E}{1 \text{ TeV}} \right)^{2.2 \pm 0.3(\text{stat.}) \pm 0.3(\text{sys.})} [\text{cm}^{-2}\text{s}^{-1}\text{TeV}^{-1}].$$

Presently we estimated the systematic errors as follows; the main one is the energy scale of 15% due to the absolute light collection efficiency and the rest is the detector systematics of 10%. The ambiguities of the absolute flux and the power-law strongly correlated to each other. The data points of Aharonian et al. (2005b) were obtained from

<http://www.mpi-hd.mpg.de/hfm/HESS/HESS.html>

Our results are consistent with H.E.S.S. for both flux level and spectrum, i.e., the CANGAROO-III results for the whole remnant yield a harder spectrum than the CANGAROO-II spectrum of Katagiri et al. (2005).

We checked the time variability of these excesses. Five periods were selected so that they have similar statistics, i.e., two-to-four days periods. The integral fluxes at energy greater than 1.02 TeV, which are normalized to the H.E.S.S. mean flux are plotted in Fig. 8. It is consistent with stable emission.

We now consider the fluxes and spectra as a function of position in the SNR to attempt to reconcile the differences between the CANGAROO-II and H.E.S.S. results. The energy spectrum obtained by CANGAROO-II is shown by the red points in Fig. 9. The CANGAROO-II flux is barely consistent with the other results. The only difference is that the single telescope CANGAROO-II observations yielded an excess only at the NW-rim. The exact procedure is reviewed as follows;

- Derive Hillas parameters and calculate *Likelihood Ratio* ( $LR$ ). Probability Density Functions (PDFs) were derived for both gamma-ray and cosmic ray initiated events. The PDFs for gamma-rays were obtained from simulations, while those for cosmic rays were obtained from OFF-source data, both in energy-by-energy bases. Histograms were made of *length* and

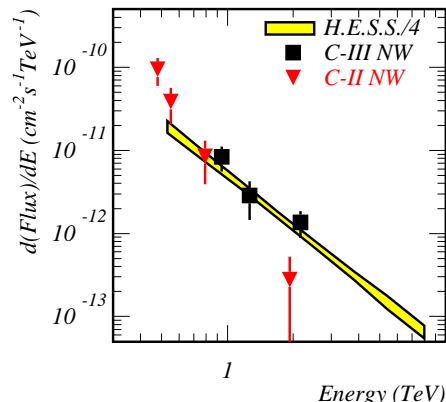


FIG. 9.— Differential energy spectra; the red points are obtained by CANGAROO-II around the NW-rim and the black points are obtained by this observation for the quadrant centered around the NW-rim. The yellow area is 1/4 of the H.E.S.S. flux.

*width* using both data sets; these distributions were then normalized to unity. The probability ( $L$ ) for each assumption was thus obtained by multiplying  $\text{PDF}(\text{width})$  by  $\text{PDF}(\text{length})$ . In order to obtain a single parameter, and also to normalize it to unity, we used the Likelihood-ratio ( $LR$ ):  $\frac{L(\text{gamma-ray})}{L(\text{gamma-ray})+L(\text{proton})}$ , therefore, in energy-by-energy bases.

- Select  $LR > 0.4$  events and plot  $Alpha$  ("Image oriented angle").
- Normalize ON- and OFF-source distributions at  $Alpha > 30$  degrees and obtain the excess within  $Alpha < 30$  degree. We did not use the time-based normalization (considering the ON- and OFF-source observation time ratios). Only the shape of the OFF-source  $Alpha$  distribution was used to determine the normalization factor.

Only in the case that the spectral index in the NW-rim is softer than elsewhere can the softer spectrum obtained by CANGAROO-II be explained. We counted the excess within the quadrant within  $\pm 45$  degree from the NW-rim center (RA, dec = 132.245°, -45.650° J2000). The result is shown by the black points in Fig. 9 which is slightly higher than 1/4 of the whole emission (the hatched area in Fig. 9). Its spectrum is still consistent with that of the whole remnant. Therefore, it is not consistent with the CANGAROO-II flux within the statistical errors. Additional systematic uncertainties such as outlined in Katagiri et al. (2005) are required. The main one was considered to be energy uncertainty due to the deterioration of mirrors and PMTs. Also saturation of the electronics might contribute. In particular, the lower energy fluxes were derived with large acceptance correction factors and have larger systematic errors.

We analyzed the same data again using a likelihood-ratio instead of the Fisher Discriminant for the

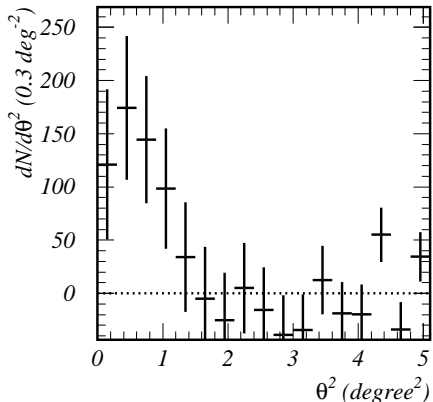


FIG. 10.— Wide range  $\theta^2$  plot obtained using the “Likelihood analysis”.

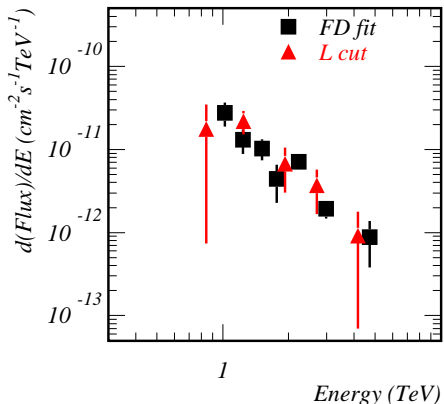


FIG. 11.— Differential energy spectra; the red points were obtained using the “Likelihood-Ratio analysis” for the whole remnant and the black points by the *FD* analysis for the the whole remnant. The error bars are statistical.

gamma/hadron separation in order to check the CANGAROO-II analysis. Here we used *lengths* and *widths* of three telescopes and used a safety cut of  $LR > 0.1$  for this supernova remnant in Fig. 10. We see a similar excess within the remnant. The number of excess events is  $538 \pm 128$  ( $4.2\sigma$ ), consistent with that obtained by the *FD* analysis. The flux obtained by this method is shown in Fig. 11. The best fit with a power-law assumption is:  $\frac{dF}{dE} = [2.4 \pm 0.8(stat.) \pm 0.6(sys.)] \times 10^{-11} \cdot \left(\frac{E}{1 \text{ TeV}}\right)^{2.0 \pm 0.4(stat.) \pm 0.3(sys.)} \text{ cm}^{-2} \text{ s}^{-1} \text{ TeV}^{-1}$ . Therefore, the detection of this supernova remnant by Katagiri et al. (2005) is shown to be correct. Hardware correction for the “light collecting” efficiencies and “saturation” effect have been refined since the CANGAROO-II results, and since the CANGAROO-II

telescope (T1) has not been operated in recent years, it is hard to estimate these deteriorations over 2001 to 2003.

## 6. DISCUSSION

We now discuss the possible origins of these TeV gamma rays. The key constraints are the energy of the protonic cosmic rays are  $\sim 10^{50}$  and the electronic  $\sim 10^{48}$  erg. The former is required for the supernova origin of cosmic rays and the ratio between the former and latter is based on the electron measurements in the solar system (Kobayashi et al. 2004). We, here, argue the distance of this SNR and the mechanism of the gamma-ray emission.

We first modeled the TeV gamma-ray flux assuming Inverse Compton scattering on the cosmic microwave background. The input electron spectrum is assumed to be proportional to  $E^{-\gamma} e^{-E/E_{max}}$ . Here the number of the data points are 16 (H.E.S.S.=9 and CANGAROO-III=7). The best-fit results under a fixed parameter of  $\gamma = 2.1$  (a typical assumption) are for an exponential cut-off energy of  $E_{max} = 26 \pm 5$  TeV with  $\chi^2/dof=13.9/(16-2)$ . Under the assumption of  $d=200$  pc (distance of this SNR from earth) we obtained total electron energy at  $E$  greater than 1 GeV of  $E_e = 0.04 \pm 0.01 \cdot 10^{48}$  erg which is low considering the supernova origin of cosmic rays under the assumption of the electron/proton ratio ( $e/p$ ) at the acceleration site (Reynolds 1996; Kobayashi et al. 2004). Note that we only consider the statistical errors of the observation. The real errors of the fitted parameters would be larger than those cited.

Second we consider protonic contributions to the TeV flux. Assuming a shock velocity of  $5000 \text{ km s}^{-1}$  in the free expansion era and a swept mass of order  $M_{\odot}$  with the age of this SNR of 630 yr ( $d=200$  pc), the ambient interstellar matter (ISM) density of  $n=0.2$  p/cc is obtained. In the case of  $d=1$  kpc,  $n=0.002$  p/cc. We carried out a two-parameter fit ( $E_{max}$  and  $E_p$ ) to only the TeV flux with a fixed parameter of  $\gamma = 2.1$  where the input proton flux was assumed again to be proportional to  $E^{-\gamma} e^{-E/E_{max}}$ . The best fit was obtained for  $E_{max} > 70$  TeV with  $\chi^2/dof = 15.2/(16-2)$ . The protonic CR energy at  $d=200$  pc is  $E_p = 0.80 \pm 0.08 \cdot 10^{50}$  erg under the assumption of the ambient ISM density of 0.2 p/cc at  $d=200$  pc. We can not reject a protonic contribution to the TeV emission for  $d=200$  pc. We, however, should have a significant electronic contribution and to produce a significant protonic component we need to suppress the  $e/p$ -ratio to far less than 0.01. When we constrain the total cosmic-ray energy to be less than  $10^{50}$  erg at  $d=1$  kpc, the ambient density of the ISM is required to be at least  $4 \text{ p/cc}$ . A total mass of  $\sim 550 \frac{n}{1 \text{ p/cc}} M_{\odot}$  within a 1 degree radius is necessary in that volume with a shell-like distribution. This kind of heavy of molecular cloud is, however, marginally within the detectable range of recent CO observations. The search for such a molecular cloud is necessary.

We now shift to the lower energy region. The radio data used here are based on Table 2 of Duncan and Green (2000) and the X-ray data are from Table 1 of Slane et al. (2001) (ASCA). Note that Slane et al. (2001) show fluxes for the north-west, north-east, and west regions of this SNR. We combined them

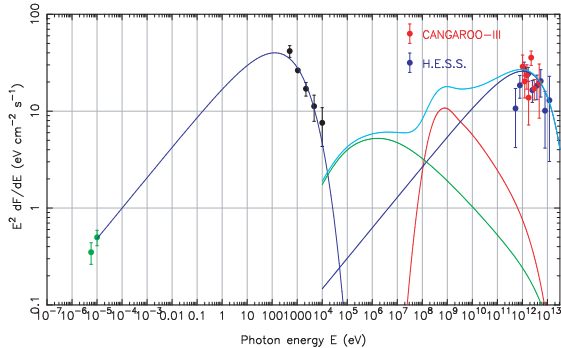


FIG. 12.— Spectral energy distributions. The data points are for radio, X-ray, H.E.S.S., and this observation. The colored curves are model calculations; the blue at low energy are for synchrotron radiation and at high energy are Inverse Compton, the red are  $\pi^0$  decay, the green, Bremsstrahlung, and the light blue show the sum at high energy.

and calculate five data points from 0.5 to 10 keV. They only gave errors for the spectral indices. We, therefore, take only them into account, i.e., the errors are underestimated. With the above best-fit parameters under the electron assumption, an ambient magnetic field of  $B \sim 4 \mu\text{G}$  also gives an allowable one-parameter fit to the X-ray spectrum and lower estimation to the radio observation.

A filamental X-ray structure was observed for this SNR by Chandra (Bamba et al. 2005). We might need to introduce a magnetic field filling factor ( $f_B < 1$ ). The best-fit results freeing all five parameters are shown in Fig. 12. The  $\chi^2/dof$  was 18.8/(23–5) with 23 data points. The fitted spectral energy distribution is shown in Fig. 12. The blue lines are the electronic contributions described above. We obtained:  $B = 5.8 \pm 0.3 \mu\text{G}$ ,  $f_B = 0.40 \pm 0.04$ ,  $\gamma = 2.37 \pm 0.01$ ,  $E_{max} = 37 \pm 2 \text{ TeV}$ , and  $E_e = 0.18 \pm 0.02 \times 10^{48} \text{ erg}$  at  $d=200 \text{ pc}$ , less energetic than that of the standard supernova origin. Also the filling factor looks too large to create the X-ray filamental structure. If this SNR is assumed to be located at  $d=1 \text{ kpc}$ , the energy simply becomes 25 times bigger, that is, marginally higher than usually assumed. This low magnetic field strength with the estimated age of 630 yr at  $d=200 \text{ pc}$  is considered to be within the allowable range for theory of electron acceleration up to 40 TeV. Assuming the proton spectrum is the same as that of the electrons and its energy is hundred times larger, the red line is the expectation of the  $\pi^0 \rightarrow \gamma\gamma$  contribution which is a negligibly small contribution to the TeV emission. The green line is that for Bremsstrahlung. Note that this calculation has a big uncertainty in the sub-MeV region. Suzaku observations of the hard-X region are eagerly awaited. In the case of  $\gamma = 2.1$ , the contribution from Bremsstrahlung is below the Suzaku sensitivity limit.

Considering the filamental structure observed in X-rays, Bamba et al. (2005) assumed a magnetic field as high as  $500 \mu\text{G}$ . This model predicted the maximum energy of the electrons to be  $E_{max} = 3 \text{ TeV}$ . With that energy spectrum, the observed flat TeV emission can not be well described via either Inverse Compton or  $\pi^0$  decay processes. In order to fit the TeV spectrum, an order of magnitude higher cut-off energy is definitely nec-

essary, which favors a two orders of magnitude lower magnetic field, because the maximum energy of the synchrotron radiation is a function of  $E_{max}\sqrt{B}$ . This contradiction can be resolved by introducing a different energy spectrum between electrons and protons as was predicted by kinetic non-linear acceleration theories where synchrotron cooling of electrons was taken into account (see for example Berezhko et al. (2003)). The filamental structure might be a result of strong synchrotron losses of emitting electrons in amplified fields as in case of other SNRs (Vink & Laming 2003; Berezhko et al. 2003; Berezhko & Völk 2004). Such a high magnetic field (hundreds of  $\mu\text{G}$ ) in the downstream region reject an Inverse Compton solution thus supporting the idea of a nucleonic origin of the observed TeV gamma-ray flux. However, in that case, we need an origin other than SNRs for the observed electrons in the solar system. Our simple estimation agrees with their models (Berezhko et al. 2003).

Although at present a perfect interpretation is missing, fine angular resolution studies over a broad energy range should help to determine one.

## 7. CONCLUSION

We have observed the supernova remnant RX J0852.0–4622 with the CANGAROO-III stereoscopic imaging Cherenkov telescope. It is clear from the results for RX J0852.0–4622 that CANGAROO-III’s stereoscopic performance is significantly improved from that of the single CANGAROO-II telescope. We have confirmed the H.E.S.S. group’s result about the morphology and the energy spectrum. The NW rim is the brightest feature. RX J0852.0–4622 has been confirmed to be one of the strongest TeV gamma-ray sources in the southern hemisphere and shows a clear shell-type structure at these energies. The energy spectrum around the NW-rim was measured to be consistent with that of the whole remnant, not in good agreement with the previous CANGAROO-II result. The difference can be partially explained by the deterioration of the hardware of the CANGAROO-II telescope.

## ACKNOWLEDGMENTS

This work was supported by a Grant-in-Aid for Scientific Research by the Japan Ministry of Education, Culture, Sports, Science and Technology, the Australian Research Council, JSPS Research Fellowships, and Inter-University Researches Program by the Institute for Cosmic Ray Research. We thank the Defense Support Center Woomera and BAE Systems.

## APPENDIX: 2004 OBSERVATION RESULTS

Additional observations were carried out in the period from 2004 January 17 to February 25 in the same “wobble mode” as the 2005 observations. The average pointing position was the NW-rim (RA, dec =  $132.245^\circ$ ,  $-45.650^\circ$  J2000), i.e., the maximum of the X-ray emission. However, only the second and third telescopes, T2 and T3, were used for the 2004 observations as T4 became operational after these observations had been completed. Also in this period the “Global Trigger” system was not ready. Data were recorded for T2 or T3 independently when the photomultiplier signals exceeded 7.6 photoelectrons (p.e.) in more than four camera pixels (“Local Trigger”).

The GPS time stamp was recorded in each dataset. An offline coincidence of time stamps from T2 and T3 within  $\pm 100 \mu\text{s}$  (Enomoto et al. 2006) was required for a stereo event. The typical trigger rate for each telescope was 80 Hz, which was reduced to 12 Hz for stereo events. The light-collecting efficiency was calibrated during the offline processing by analyzing  $\mu$ -rings and found to be  $70 \pm 5\%$  for both T2 and T3, as for the Vela Pulsar observations (Enomoto et al. 2006). The total observation time was 1781, and 436 min, for ON- and OFF-source data, respectively. After pre-selection, the event rate was reduced to 10 Hz. Finally after the “cloud and elevation cut” the analyzable data (ON-source run) corresponded to 1120 min. with a mean elevation angle of  $70.3^\circ$ . The OFF-source data, however, only had 379 min., in part as these observations were carried out at a similar time with the CANGAROO-III observations of the Vela pulsar region described by Enomoto et al. (2006).

The differences between these and 2005 data are summarized as follows;

- 2-fold (software) coincidence in 2004 and 3-fold (hardware) coincidence in 2005, and
- the OFF-source data in 2004 are only 1/3 of the ON-source data,

Although the light collecting efficiency is higher than 2005, there remain some uncertainties, especially in the background subtraction. We, therefore, report these results in this Appendix as supporting evidence to the main

arguments.

The same kind of analysis as for the 2005 data were carried out. Here, we restrict the analysis only to the higher acceptance regions due to the lack of statistics in OFF-source runs. The higher acceptance region was chosen as within 1.4 degrees from each “wobble” pointing. Only the overlapping region was analyzed. This is approximately the north-east half of the remnant. Comparing with the 3-fold data, the signal-to-noise ratio is poor. The 3-fold coincidence data had better background rejection power than that of the 2-fold data. The errors in the subtracted data are dominated by the OFF-source statistical errors. Due to these, the statistically accurate background functions could not be obtained position-by-position bases in the FOV. The background also behaved non-uniformly near the edge of the camera. Therefore, we did not use the fitting procedure of the 2005 analysis. The ON–OFF subtraction was carried out using time-based normalization factor.

As has been described, we can only analyze half of the remnant. The flux inside the maximum acceptance region is shown in Fig. 13, i.e., fluxes of the half remnant. The energy resolution was estimated using Monte-Carlo simulations in the same way as the 2005 analysis to be  $\Delta E/E = 17/\sqrt{E/1 \text{ TeV}} + 12\%$ , which is slightly worse than the 3-fold analysis. The energy spectrum is similar and the flux is half compared to the whole remnant. This is supporting evidence for the results of the 2005 observations.

## REFERENCES

- Abe, K., et al. 2001, Phys. Rev. Lett., 87, 101801  
 Aharonian, F. A., et al. 1999, A&A, 349, 11  
 Aharonian, F. A., et al. 2004, Nature, 432, 75  
 Aharonian, F. A., et al. 2005, Science, 307, 1938  
 Aharonian, F. A., et al. 2005b, A&A, 437, L7  
 Aschenbach, B. 1998, Nature, 396, 141  
 Aschenbach, B., Iyudin, A. F., & Schönfelder, V. 1999, A&A, 350, 997  
 Bamba, A., Yamazaki, R., Hiraga, J. S. 2005, ApJ, 632, 294  
 Berezhko, E. G., Ksenofontov, L. T., & Völk, H. J., 2003, A&A, 412, L11  
 Berezhko, E. G., & Völk, H. J., 2004, A&A, 419, L27  
 Daum, A., et al. 1997, Astropart. Phys., 8, 1  
 Duncan, A. R., and Green, D. A., 2000, A&A, 364, 732  
 Enomoto, R., et al. 2002b, Nature, 416, 823  
 Enomoto, R., et al. 2002a, Astropart. Phys., 16, 235  
 Enomoto, R., Tsuchiya, K., Adachi, Y., Kabuki, S., Edwards, P. G., et al. 2006, ApJ, 638, 397  
 Fisher, R. A. 1936, Annals of Eugenics, 7, 179  
 Hillas, A. M. Proc. 19th Int. Cosmic Ray Conf. (La Jolla) 3, 445  
 Hofmann, W., et al. 2000, Astropart. Phys., 12, 207  
 Kabuki, S., et al. 2003, Nucl. Instrum. Meth., A500, 318  
 Katagiri, H., Enomoto, R., Ksenofontov, L. T., Mori, M., et al. 2005, ApJ, 619, L163  
 Kawachi, A., et al. 2001, Astropart. Phys., 14, 261  
 Kobayashi, T., Komori, Y., Yoshida, K., Nishimura, J. 2004, ApJ, 601, 340  
 Nishijima, K., et al. 2005, Proc. 29th Int. Cosmic Ray Conf. (Pune), OG2.7, 101  
 Reynolds, S. P. 1996, ApJ, 459, L13  
 Slane, P., et al. 2001, ApJ, 548, 814  
 Tanimori, T., et al. 2005, Proc. 29th Int. Cosmic Ray Conf. (Pune), OG2.2, 215  
 Tsunemi, H., et al. 2000, PASJ, 52, 887  
 Vink, J. & Laming, J. M., 2003, ApJ, 548, 758  
 Völk, H. J., Berezhko, E. G., & Ksenofontov, L. T. 2005, A&A, 433, 229

- Weekes, T. C., et al. 1989, ApJ, 342, 379

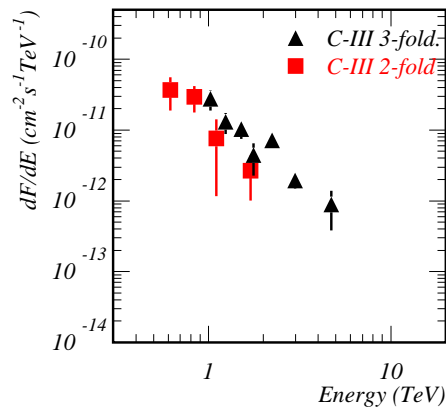


FIG. 13.— Differential energy spectra; the black points from the 3-fold coincidence analysis of 2005 CANGAROO-III data for the whole remnant (the same as the black points in Fig. 7, and the red points from the 2-fold analysis of 2004 CANGAROO-III for about a half of the remnant.